The basis for non-canonical ROK family function in the *N*-acetylmannosamine kinase from the pathogen *Staphylococcus aureus*

Received for publication, August 8, 2019, and in revised form, December 31, 2019 Published, Papers in Press, January 15, 2020, DOI 10.1074/jbc.RA119.010526

David Coombes[‡], James S. Davies[‡], Michael C. Newton-Vesty[‡], Christopher R. Horne[‡], Thanuja G. Setty[§¶], Ramaswamy Subramanian[§], James W. B. Moir[‖], Rosmarie Friemann[**‡‡], Santosh Panjikar[§§¶¶], Michael D. W. Griffin[‖‖], Rachel A. North[‡1], and Renwick C. J. Dobson[‡‖‖2]

*From the [‡]Biomolecular Interaction Centre and School of Biological Sciences, University of Canterbury, Christchurch 8140, New Zealand, the [§]Institute for Stem Cell Biology and Regenerative Medicine, NCBS, GKVK Campus, Bellary Road, Bangalore, Karnataka 560 065, India, [¶]The University of Trans-Disciplinary Health Sciences and Technology (TDU), Bangalore, KA 560064, India, the [‖]Department of Biology, University of York, Helsington, York YO10 5DD, United Kingdom, the **Department of Clinical Microbiology, Sahlgrenska University Hospital, Guldhedsgatan 10A, 413 46 Gothenburg, Sweden, the [‡‡]Centre for Antibiotic Resistance Research (CARe), University of Gothenburg, 40530 Gothenburg, Sweden, the [§§]Department of Biochemistry and Molecular Biology, Monash University, Clayton, Victoria 3800, Australia, the [¶¶]Australian Synchrotron, ANSTO, Victoria 3168, Australia, and the [‖‖]Department of Biochemistry and Molecular Biology, Bio21 Molecular Science and Biotechnology Institute, University of Melbourne, Parkville, Victoria 3010, Australia*

Edited by Joseph M. Jez

In environments where glucose is limited, some pathogenic bacteria metabolize host-derived sialic acid as a nutrient source. *N*-Acetylmannosamine kinase (NanK) is the second enzyme of the bacterial sialic acid import and degradation pathway and adds phosphate to *N*-acetylmannosamine using ATP to prime the molecule for future pathway reactions. Sequence alignments reveal that Gram-positive NanK enzymes belong to the Repressor, ORF, Kinase (ROK) family, but many lack the canonical Zn-binding motif expected for this function, and the sugar-binding E*X*GH motif is altered to E*X*GY. As a result, it is unclear how they perform this important reaction. Here, we study the *Staphylococcus aureus* NanK (*Sa*NanK), which is the first characterization of a Gram-positive NanK. We report the kinetic activity of *Sa*NanK along with the ligand–free, *N*-acetylmannosamine–bound and substrate analog GlcNAc–bound crystal structures (2.33, 2.20, and 2.20 Å resolution, respectively). These demonstrate, in combination with small-angle X-ray scattering, that *Sa*NanK is a dimer that adopts a closed conformation upon substrate binding. Analysis of the E*X*GY motif reveals that the tyrosine binds to the *N*-acetyl group to select for the "boat" conformation of *N*-acetylmannosamine. Moreover, *Sa*NanK has a stacked arginine pair coordinated by negative residues critical for thermal stability and catalysis. These combined elements serve to constrain the active site and orient the substrate in lieu of Zn binding, representing a significant departure from canonical NanK binding. This characterization provides insight into differences in the ROK family and highlights a novel area for antimicrobial discovery to fight Gram-positive and *S. aureus* infections.

Pathogenic bacteria import and utilize a wide variety of carbohydrates. In environments where glucose is limited, amino sugars such as sialic acids are important nutrient sources. In general, the bacterial sialic acid catabolic pathway is a validated antimicrobial target (1–4), because sialic acids are scavenged from mucins that coat the gastrointestinal and respiratory tracts of humans (5) and are imported (6–8) and used by pathogenic bacteria as a carbon, nitrogen, and energy source when they colonize these niches (1, 9–11). This is particularly the case in mucosal surfaces, where the amino sugar GlcNAc and the sialic acid, *N*-acetylneuraminate, are widely incorporated into glycoconjugate mucins and cell surfaces (1). These carbohydrates can be scavenged from host glycoconjugates and metabolized by mucosal pathogens, such as *Staphylococcus aureus* (2), as a nutrient source (3–6).

Just as the phosphorylation of glucose in the early phase of glycolysis (sometimes referred to as the "energy investment phase") drives otherwise unfavorable reactions in the payoff phase as glucose is catabolized, in the bacterial sialic acid import and degradation pathway (Fig. 1*A*), phosphorylation serves to prime the amino sugar for downstream catabolism

This work was supported by in part by New Zealand Royal Society Marsden Fund contract UOC1506, Ministry of Business, Innovation and Employment Smart Ideas Grant UOCX1706, and the Biomolecular Interactions Centre (University of Canterbury) (to R. C. J. D.), Australian Research Council Future Fellowship project FT140100544 (to M. D. W. G.), University of Canterbury Doctoral Scholarships (to D. C. and R. A. N.), New Zealand Royal Society Marsden Fund contract UOC1506 (to R. A. N.), DBT-Indo Swedish Grant BT/IN/SWEDEN/06/SR/2017-18 (to R. S. and T. G. S.), a Senior Research fellowship from the Council of Scientific and Industrial Research (CSIR) (to T. G. S.), Swedish Governmental Agency for Innovation Systems (VINNOVA) Grant 2017-00180 (to R. F.) and the Centre for Antibiotic Resistance Research (CARe) at University of Gothenburg (to R. F.), and an Erskine distinguished Visiting Fellowship (to J. W. B. M.). The authors declare that they have no conflicts of interest with the contents of this article.
This article contains Figs. S1–S13 and Table S1.
The atomic coordinates and structure factors (codes 6Q26, 6Q27, and 6Q28) have been deposited in the Protein Data Bank (http://wwpdb.org/).
[1] To whom correspondence may be addressed: P.O. Box 4800, Christchurch 8140, New Zealand. Tel.: 64-3-364-2987; E-mail: rachel.north@dbb.su.se.
[2] To whom correspondence may be addressed: Biomolecular Interaction Centre and School of Biological Sciences, University of Canterbury, Christchurch, New Zealand. Tel.: 64-3-369-5145; E-mail: renwick.dobson@canterbury.ac.nz.

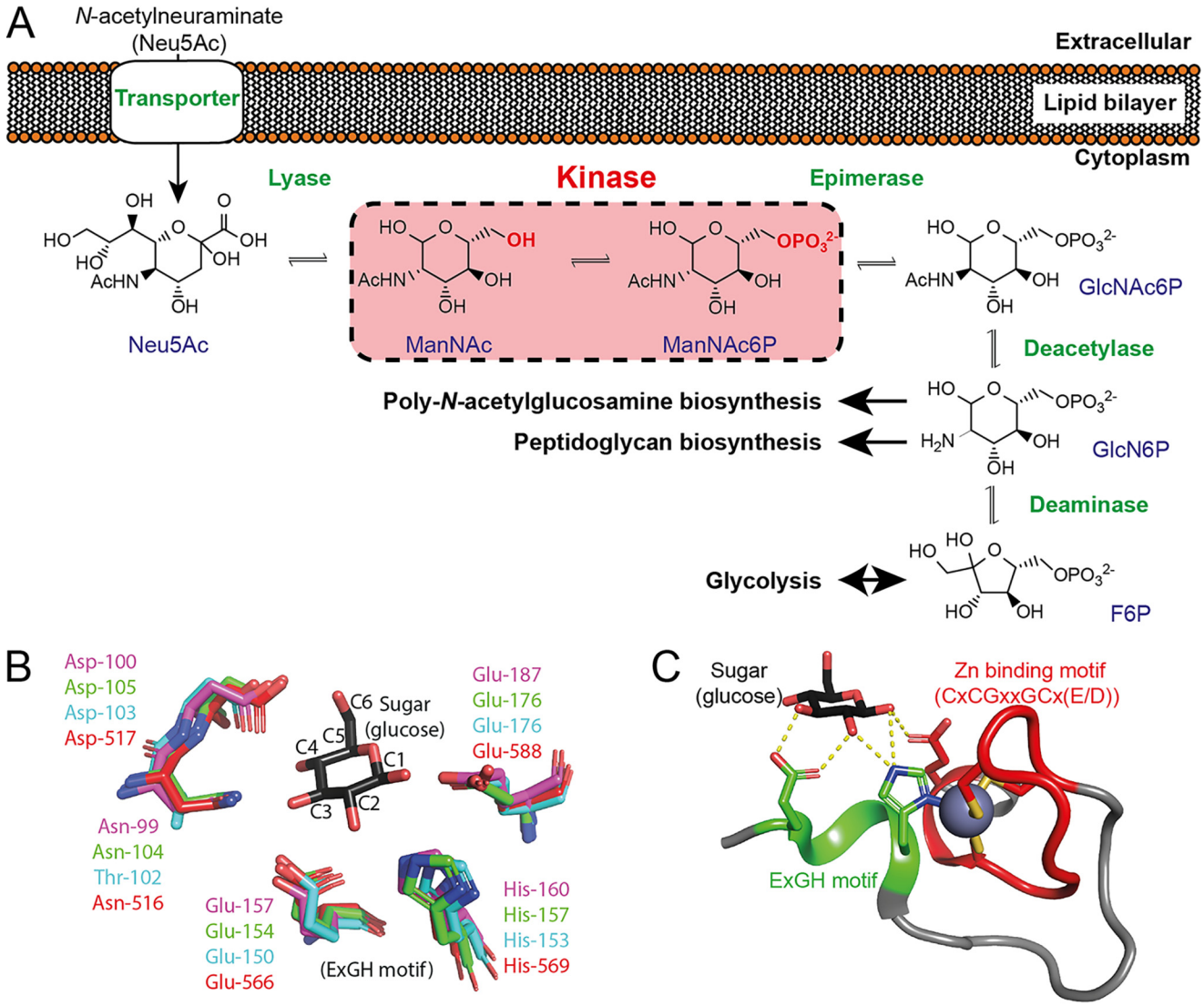

Figure 1. *A,* a schematic of sugar flow through the bacterial sialic acid catabolism pathway. NanK catalyzes the conversion of *N*-acetylmannosamine and ATP to form *N*-acetylmanosamine-6-phosphate and ADP. This proposed pathway is based on experimental evidence from *S. aureus* (4), *Bacillus subtilis* and *Escherichia coli* (55), as well as from KEGG genome data (56). For clarity, substrate and enzyme names are abbreviated. Enzymes used were: sialic acid transporter (6–8), *N*-acetylneuraminate lyase (57, 58), *NanK*, *N*-acetylmannosamine-6-phosphate 2-epimerase (59, 60), GlcNAc-6-phosphate deacetylase, and glucosamine-6-phosphate deaminase (12). Substrates used were: *N*-acetylneuraminate, *N*-acetylmannosamine, *N*-acetylmannosamine-6-phosphate, GlcNAc-6-phosphate, glucosamine-6-phosphate, and fructose-6-phosphate. *B,* structures of sugar-bound ROK and non-ROK sugar kinases have a highly-conserved sugar-binding site. Glucokinase family *E. coli* glucokinase is shown in *pink* (PDB 1SZ2), ROK *S. griseus* glucokinase in *green* (PDB 3VGL), ROK *B. subtilis* fructokinase in *cyan* (PDB 3LM9), and ROK human bi-functional UDP-GlcNAc 2-epimerase/NanK in *red* (PDB 2YHY). *C,* this image shows the orientation of the EXGH motif (*green*) and ROK Zn-binding motif (*red*) relative to the sugar-binding site (PDB 3VGL).

through glycolysis, or anabolism by synthetic pathways, including cell wall synthesis (10, 12). Here, we focus on the second step of the catabolic pathway: the phosphorylation of *N*-acetylmannosamine catalyzed by *N*-acetylmannosamine kinase (henceforth abbreviated to NanK).

In bacteria, enzymes from two distantly related protein families carry out ATP-driven sugar phosphorylation (13): the glucokinase family (14) and the Repressor, ORF, Kinase (ROK)[3] family (15). Both families have the RNase H-like protein-fold, a sugar substrate-induced conformational change, ATP-binding D*X*G*X*T and GTG*X*G motifs, and a sugar-binding E*X*GH motif (13, 15). The sugar substrate-binding site is also somewhat conserved, with ligand–bound crystal structures showing five conserved sugar-binding residues (Fig. 1*B*) (13). The key difference between the families is that ROK proteins have a Zn-binding motif (C*X*CG*XX*GC*X*(E/D)) that buttresses the E*X*GH motif histidine, placing it in the correct position for substrate binding (Fig. 1*C*). In contrast, the glucokinase family lack the Zn-binding motif and instead have an additional α-helix to structure the region (16).

We conducted a sequence alignment of NanK enzymes from bacteria, which are expected to be part of the ROK family (13). Curiously, we found that the majority of Gram-positive bacterial NanK sequences lack the Zn-binding motif and the α-helix used in the glucokinase family (Fig. S1). This is best shown in an alignment of representative NanK sequences (Fig. S2), which reveals that the cysteine residues usually involved in forming

[3] The abbreviations used are: ROK, repressor, ORF, kinase; PDB, Protein Data Bank; RMSD, root mean square deviation.

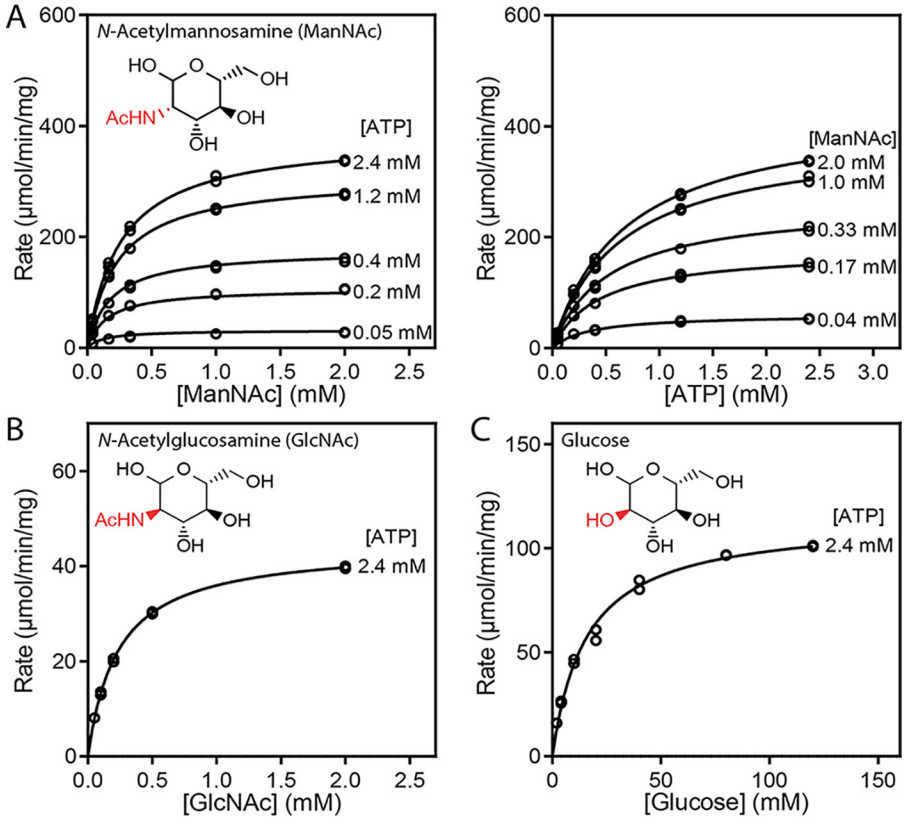

Figure 2. Kinetic assays with *N*-acetylmannosamine kinase. *A,* rate *versus* *N*-acetylmannosamine and ATP concentration fitted with the ternary complex kinetic model: K_m (*N*-acetylmannosamine) = 0.30 ± 0.01 mM, $K_m^{(ATP)}$ = 0.7 mM, V_{max} = 497 ± 7 μmol/min/mg, k_{cat} = 263 ± 3 s^{-1}. *B,* rate *versus* GlcNAc concentration fitted to the Michaelis-Menten model: K_m^{app} = 0.26 mM, V_{max} = 114 μmol/min/mg, k_{cat}^{app} = 23.4 ± 0.2 s^{-1}. *C,* rate *versus* glucose concentration fitted to the Michaelis-Menten model: K_m = 15 ± 1 mM, V_{max} = 44.4 ± 0.3 μmol/min/mg, k_{cat} = 60 ± 1 s^{-1}.

the Zn-binding motif are absent in sequences of Gram-positive *S. aureus* and *Streptococcus mitis* species, and the histidine of the E*X*GH motif is substituted with a tyrosine (E*X*GY) (17). This is surprising, as Zn-binding is required for activity in ROK proteins (15, 18), is present throughout Gram-negative NanK isozymes (13, 19), and the Zn-binding motif differentiates the ROK family from the glucokinase family (15).

Given that many Gram-positive NanK enzymes have been traditionally annotated as ROK enzymes, but are missing the essential Zn-binding motif, and instead have a tyrosine in place of histidine from the sugar-binding E*X*GH motif, we studied how Gram-positive *S. aureus* NanK (*Sa*NanK) functions without these canonical features. Here we report the first functional and structural study of a Gram-positive NanK. We discovered that the enzyme is active without Zn-binding, has a unique structured arginine π-stack in a position equivalent to the ROK Zn-binding motif, or glucokinase family α-helix, and that the tyrosine in the E*X*GY motif provides specificity for the *N*-acetylmannosamine substrate.

Results and discussion

SaNanK N-*acetylmannosamine kinase catalytic function*

We first verified whether *Sa*NanK was a *N*-acetylmannosamine kinase using an established assay for measuring initial rate data (19). The enzyme is active with *N*-acetylmannosamine and ATP. Initial rate data, where both acetylmannosamine and ATP concentrations are varied, are best fitted with the ternary complex kinetic model (Fig. 2*A*), with an R^2 = 0.999 (see "Experimental procedures" for a discussion on how this model was chosen). This gives the following kinetic parameters: $K_m^{N\text{-acetylmannosamine}}$ = 0.30 mM, K_m^{ATP} = 0.73 mM, and k_{cat} = 262.6 s^{-1} (V_{max} = 497 μmol min^{-1} mg^{-1}) (Table 1). The k_{cat}/K_m for *N*-acetylmannosamine is 870 mM^{-1} s^{-1}, which is on the same order as the only other *bona fide* bacterial NanK enzyme characterized (from *Escherichia coli*) (19), and other ROK kinases (19–23). Thus, *Sa*NanK is catalytically active and kinetically comparable with other ROK kinases, despite missing conserved and defining active site motifs thought to be important for function.

Three ROK *Streptomyces* glucokinases have been reported to have a compulsory-ordered mechanism, where glucose binds the active site before ATP (16, 24). When the initial rate data are presented as double-reciprocal plots the pattern provides information on whether the ternary complex kinetic mechanism is of the random- or compulsory-ordered type with respect to substrate binding (25). The plots for *Sa*NanK are consistent with a random-ordered ternary complex for catalysis (Fig. S5). These results demonstrate that *Sa*NanK binds substrate differently than *Streptomyces* ROK glucokinases, which presumably have a structural feature that prevents ATP from binding first.

Glucose kinase activity is thought to be the ancestral function for the ROK family (13). Glucose differs from *N*-acetylmannosamine in that a equatorial (*R*)-hydroxyl at the C2 position is substituted with an axial (*S*)-*N*-acetyl group. To probe substrate specificity for the C2 position, we compared the catalytic func-

Table 1
Kinetic parameters for wildtype *Sa*NanK

The V_{max}, k_{cat}, and K_m were calculated in GraphPad Prism. The error is the mean ± S.E. of the fit. *N*-Acetylmannosamine parameters were produced from global fits by varying ATP.

	N-Acetylmannosamine	Glucose[a]	GlcNAc[a]
V_{max} (μmol/min/mg)	497 ± 7	114 ± 3	44.4 ± 0.3
k_{cat} (s^{-1})	263 ± 3	60 ± 1	23.4 ± 0.2
K_m (mM)	0.30 ± 0.01	15 ± 1	0.260 ± 0.005
k_{cat}/K_m (s^{-1}/mM)	871 ± 34	4.0 ± 0.3	90 ± 3
ATP K_m (mM)	0.73 ± 0.02		

[a] Glucose and GlcNAc are apparent parameters, using a saturating ATP concentration.

tion with *N*-acetylmannosamine against glucose and GlcNAc, which are C2 substrate analogs. The apparent K_m (K_m^{app}) of GlcNAc (260 μM) is comparable with *N*-acetylmannosamine (300 μM) (Fig. 2*B*). However, the k_{cat} (23 s^{-1}) is 11-fold lower. The K_m^{app} for glucose (15 mM, Fig. 2*C*) is 60-fold higher than the *N*-acetyl substrates, highlighting that the C2 *N*-acetyl group is important for binding to the enzyme. In ROK glucokinases, the C2 position is bound by the E*X*GH motif histidine (13), which in *Sa*NanK is changed to tyrosine and represents an uncharacterized change within the ROK protein family. This result demonstrates that the *N*-acetyl substrate group is important for substrate binding and consequently the residues of the enzyme that coordinate the *N*-acetyl are important for substrate specificity.

Overall, we demonstrate that *Sa*NanK is a *bona fide N*-acetylmannosamine kinase with catalytic constants comparable with canonical ROK kinases that have the E*X*GH and Zn-binding motif. We show that *Sa*NanK catalysis has a random-ordered ternary mechanism, in contrast to *Streptomyces* glucokinases, which bind glucose first. The difference in kinetic mechanism suggests that *Sa*NanK has novel structural features, which may be related to the altered protein sequence. We also demonstrate that the C2 *N*-acetyl group of the substrate is important for substrate binding.

Structure of SaNanK

To investigate the structural implications of the missing canonical ROK motifs and the altered kinetic mechanism relative to other glucokinases, we solved the crystal and solution structure of *Sa*NanK in the ligand–free, *N*-acetylmannosamine– bound, and GlcNAc– bound forms. The ligand-free structure was solved to 2.33 Å resolution. Because we were unable to solve the structure using molecular replacement, selenomethionine-substituted enzyme was crystallized as previously described (17) and initial phases were determined using *SHELX* (26). The asymmetric unit contains four NanK monomers where chains A, B, and C are complete, but chain D has three regions where electron density is ambiguous and cannot be modeled (Gln-28–Pro-33, Pro-82–Pro-85, Asn-142–Gln-144). *N*-Acetylmannosamine– bound and GlcNAc– bound *Sa*NanK structures were each solved at 2.20 Å resolution, using the ligand-free structure for molecular replacement. Electron density was present and distinguishable for all residues, except Met-1. The data collection and refinement statistics are given in Table 2.

The SaNanK monomer

The *Sa*NanK monomer features two domains, an N-terminal α/β domain (Fig. 3*A*, *red*) and a larger α+β domain (Fig. 3*A*, *pink*) that together form the RNase H-like–fold. The domains are orientated such that the monomer resembles an open clam, with the two separated domains being joined at a single hinge region (Fig. 3*A*, *green*). The active site is situated between the two "half-shell" domains, where residues from both domains are used to bind substrate and support catalysis. The structure is consistent with canonical ROK kinases, with the secondary structure regions matching *E. coli* NanK (Fig. S6) and comparison with TM-align (27) provides a structure match score of 84.4 and 86.6% with *E. coli* NanK (PDB 2AA4) and *Streptomyces griseus* glucokinase (PDB 3VGK), respectively.

The active sites of ROK kinases are generally well-conserved (13). Mapping the sequence alignment to the structure demonstrates that it is the most highly-conserved area of *Sa*NanK (Fig. 3*B*). However, from our sequence analysis, there is a major change to the region with the absence of a Zn-binding motif, which in canonical ROK partially encloses the active site from the sugar side (PDB 3VGL). In *Sa*NanK, the region equivalent to the Zn-binding motif is shorter (13 *versus* 20 residues) and is folded away from the active site area, interacting with residues of the large α+β domain.

SaNanK is a dimer, consistent with other NanK enzymes

To determine the relevant oligomeric state in solution, sedimentation velocity analytical ultracentrifugation and small angle X-ray scattering experiments were conducted. Both experiments demonstrate that *Sa*NanK is a dimer (across the concentration range tested).

Sedimentation velocity data were fit with the *c*(*s*) and *c*(*M*) models using *SEDFIT* (28), which give a single peak corresponding to 3.95 S and 62 kDa (Fig. 4*A*); thus, ligand-free *Sa*NanK is a dimer in solution given a monomeric mass of 31.7 kDa calculated from the sequence. A single peak is evident at each concentration, suggesting that the equilibrium constant for dimer dissociation (K_D^{2-1}) is very low. Small angle X-ray scattering data are also consistent with a dimer. The theoretical scatter for the ligand-free *Sa*NanK canonical dimer formed in the crystal structure (generated by *CRYSOL* from the *ATSAS* package (29)) fitted closely to the scattering data ($\chi^2 = 1.7$) (Fig. 4*B*). We also tested a possible dimer formed by a secondary interface in the asymmetric unit (as defined by *PDBe PISA* (30), and the full asymmetric unit of the ligand-free structure (two dimers) (Fig. S7), both of which fitted poorly to the scattering data. The dimeric configuration is consistent with other NanK crystal structures (19, 31, 32) and MALDI-TOF MS analysis of (ROK) glucokinase from *Bacillus subtilis* (15).

From the crystal structure, the dimeric configuration orients the active sites facing outward on opposite sides of the assembly, whereas the hinge regions are near the center (Fig. 4*C*). Residues

Table 2
Data collection and refinement statistics

	Ligand-free	*N*-Acetylmannosamine-bound	GlcNAc-bound
PDB	6Q26	6Q27	6Q28
Wavelength	0.9724	0.954	0.954
Resolution range	48.736–2.328 (2.412–2.328)	44.556–2.200 (2.279 2.200)	47.88–2.2 (2.279–2.200)
Space group	$C\,2\,2\,2_1$	$P\,2_1$	$P\,2_1$
Unit cell	116.7, 135.2, 175.3	47.2, 101.4, 133.2; 90.15	47.9, 102.0, 133.3; 90.14
Total reflections	867,330 (83,021)	124,343 (11,758)	255,819 (25,619)
Unique reflections	59,453 (5,864)	63,756 (6,331)	64,898 (6,477)
Multiplicity	14.6 (14.2)	2.0 (1.9)	3.9 (4.0)
Completeness (%)	99.9 (99.4)	99.9 (99.9)	99.8 (99.5)
Mean I/sigma(I)	20.0 (1.9)	4.9 (1.0)	5.3 (0.9)
Wilson B-factor	30.98	43.34	30.46
R_{merge}	0.237 (1.557)	0.083 (0.523)	0.315 (0.692)
R_{meas}	0.245 (1.615)	0.117 (0.740)	0.368 (0.804)
R_{pim}	0.064 (0.424)	0.083 (0.523)	0.187 (0.405)
$CC_{1/2}$	0.994 (0.671)	0.988 (0.704)	0.881 (0.701)
Reflections used in refinement	59,447 (5864)	63,746 (6330)	64,886 (6477)
Reflections used for *R*-free	6,036 (622)	6,340 (603)	3,202 (315)
R_{work}	0.1973 (0.2711)	0.1940 (0.3098)	0.2198 (0.3312)
R_{free}	0.2400 (0.3284)	0.2324 (0.3362)	0.2400 (0.3480)
Number of non-hydrogen atoms	9,103	8,989	9,230
Macromolecules	8,808	8,840	8,896
Ligands	NA[a]	60	60
Solvent	295	89	274
Protein residues	1,131	1,140	1,144
RMSD (bonds)	0.009	0.009	0.016
RMSD (angles)	1.30	1.27	1.77
Ramachandran favored, allowed, outliers (%)	98.3, 1.7, 0	98.1, 1.9, 0	98.2, 1.7, 0.1
Rotamer outliers (%)	0	0.64	0.53
Average B-factor (Å^2)	37.1	51.9	38.3
Macromolecules	37.3	51.8	37.9
Ligands	NA	69.8	55.1
Solvent	32.3	55.6	48.3
Number of TLS groups	15	16	24
Anomalous completeness (%)	99.9 (98.3)		
Anomalous multiplicity	7.6 (7.2)		

[a] NA, not applicable.

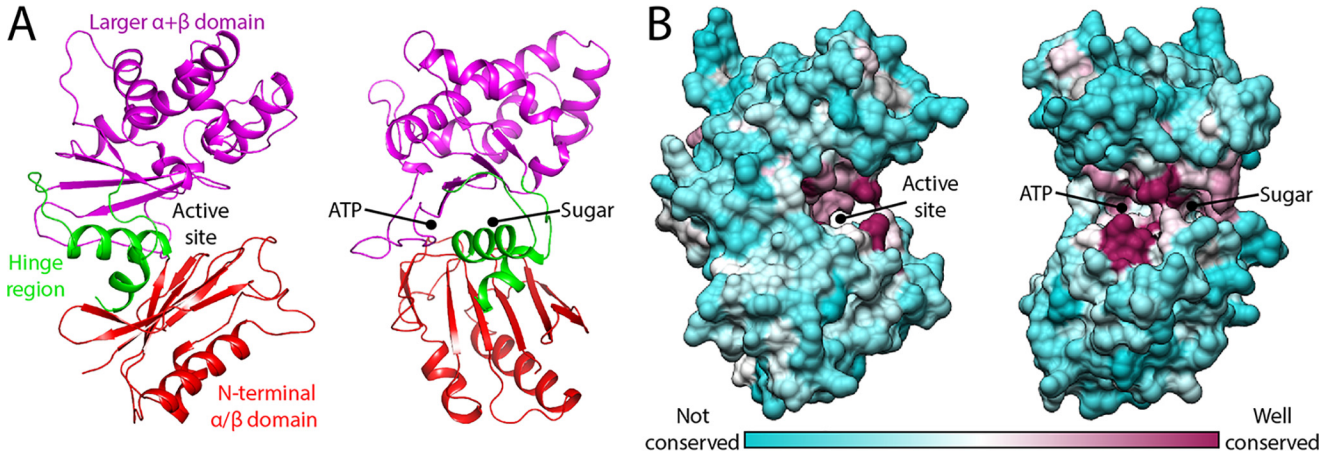

Figure 3. Monomeric structure of *Sa*NanK. *A,* the monomer has two domains: an N-terminal α/β domain (*red*) and a larger $\alpha+\beta$ domain (*pink*). The hinge region (*green*) joins the two domains and involves two α-helices shared between the domains. The active site is opposite the hinge region between the two domains. *B,* the active site residues of ROK kinases are highly conserved. Sequence alignment of ROK kinases listed in Table S1. Active sites residues are highly conserved (*maroon*) and residues elsewhere are poorly conserved (*cyan*). Image produced using *ConSurf* (62) and *UCSF Chimera* software (63).

from the large $\alpha+\beta$ domain form the dimerization interface. This configuration is consistent with *E. coli*, *Fusobacterium nucleatum,* and Homo sapiens (19, 31, 32). *PDBe PISA* analysis indicates that the *Sa*NanK interface has a surface area of 1533.8 Å^2, featuring five salt bridges and 18 hydrogen bonds. The residues identified by *PDBe PISA* contribute to three positive and three negatively charged regions that charge complement the opposing monomer (Fig. 4*D*).

In summary, we demonstrate that *Sa*NanK is a dimer. The dimeric interface consists of three complementary positive and negative patches on the surface of large $\alpha+\beta$ domain.

Substrate-induced changes in conformation

A conformational change upon sugar binding, whereby the lobes of the enzyme close over the substrate, has been demonstrated in both the ROK and glucokinase families (14, 16, 31). Whether *Sa*NanK undergoes a similar conformational change was determined by comparing the sugar substrate–bound and ligand-free X-ray crystal structures. In the *N*-acetylmannosamine–bound *Sa*NanK structure the two domains are shifted 7 Å inwards and close around the substrate, like the shells of a clam enclosing a pearl (Fig. 5*A*). As a dimer, the

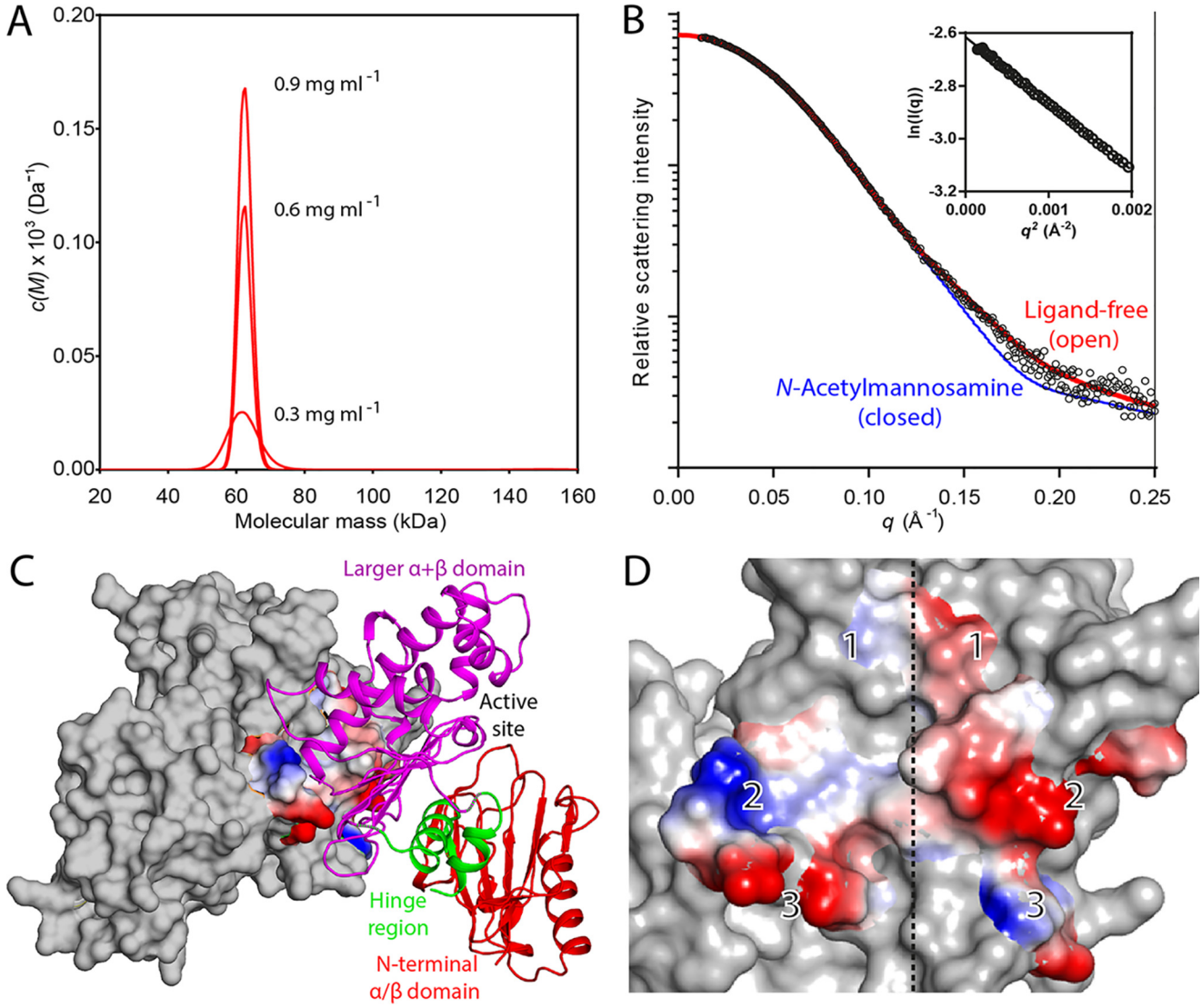

Figure 4. Oligomeric state of *Sa*NanK. *A,* sedimentation velocity experiments with *Sa*NanK at three concentrations (0.3, 0.6, and 0.9 mg ml^{-1}; 9.5, 18.9, and 27.4 μM). The fit of the model to the data (Fig. S4) provides a molecular mass of ~62 kDa, corresponding to a dimer (monomer mass is 31.7 kDa). *B,* small-angle X-ray scattering of *Sa*NanK (6 mg ml^{-1}). Ligand-free *Sa*NanK experimental data (*red circles*) corresponds with theoretical scatter (*red line*), with a reduced χ^2 of 1.7 *versus* 4.9, compared with the *N*-acetylmannosamine crystal structure scatter (*blue line*). *C,* structure of the *Sa*NanK dimer, which is formed through residues of the larger $\alpha+\beta$ domain (*pink*), with the hinge region (*green*), and large N-terminal α/β domain (*red*) free in solution. *D,* the dimeric interface of *Sa*NanK. The electrostatic surface (generated using *PyMOL*) shows three opposing negative and positive areas, which pair when the dimer interface forms. Residues involved with dimerization were determined using *PDBe PISA* and were mapped onto the surface of *Sa*NanK.

movement occurs mainly in the N-terminal α/β domain, pivoting at the hinge region, as the large $\alpha+\beta$ domain is set by the dimeric interface. Overall, the conformational change of *Sa*NanK is consistent with other ROK kinases (14, 16, 31).

The purpose of a conformational change is hypothesized to ensure that ATP hydrolysis occurs only when sugar substrate is present, providing efficient catalysis (31). To investigate, the catalytic residues identified from the sequence alignment (Fig. S2) were compared between ligand–free and *N*-acetylmannosamine–bound structures. In the catalytic mechanism for sugar kinases, ATP is primed for nucleophilic attack at the γ-phosphate by electron withdrawal through the β-phosphate, which then undergoes nucleophilic attack by the sugar (31). For *Sa*NanK, electron withdrawal likely occurs via Asp-7 binding Mg^{2+} associated with the ATP β-phosphate, given its proximity, whereas Thr-11 and Thr-134 hydrogen bond with the other side of the β-phosphate group. Alignment of Mg·ADP from the human NanK structure demonstrates that when *N*-acetylmannosamine is bound, Thr-134 is shifted toward the expected β-phosphate position (Fig. 5*B*, *pink*) and both Asp-7 and Thr-11, which are part of the N-terminal α/β domain, make a large shift toward the ATP position (Fig. 5*B*, *red*). Importantly, this shows that Asp-7, Thr-11, and Thr-134 are in position to provide electron withdrawal in the *N*-acetylmannosamine–bound structure and not the ligand-free structure. In short, this is consistent with a conformational change that ensures ATP is only hydrolyzed in the presence of substrate (discussed in Ref. 31).

As conformational change is important for catalysis in ROK kinases (discussed above), the GlcNAc and *N*-acetylmannosamine–bound structures were compared to ration-

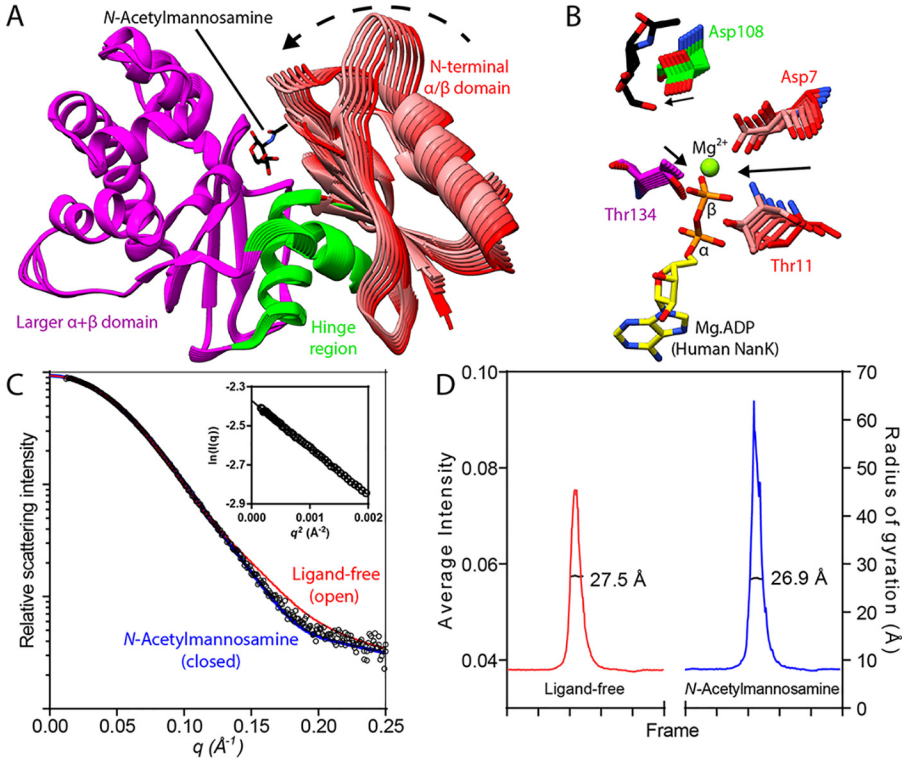

Figure 5. Conformational change in *Sa*NanK. *A,* comparison of ligand–free and *N*-acetylmannosamine–bound structures demonstrates that the N-terminal α/β domain (*red* to *white*) closes around *N*-acetylmannosamine, pivoting at the hinge region (*green*). *B,* expected catalytic residues of *Sa*NanK. The N-terminal α/β domain moves bringing Asp-7 and Thr-11 toward the active site, which in conjunction with Thr-134 prime ATP for nucleophilic attack. The expected position of ATP was indicated by aligning the human NanK structure with *N*-acetylmannosamine and Mg·ADP bound (PDB 2YHY). Asp-108 binds and deprotonates the C6 hydroxyl of *N*-acetylmannosamine, increasing nucleophilicity of the sugar. *C,* small-angle X-ray scattering of *Sa*NanK (6 mg ml^{-1}) and *N*-acetylmannosamine (5 mM). Experimental data (*blue circles*) corresponds with theoretical scatter of the *N*-acetylmannosamine-bound crystal structure (*blue line*), with a reduced χ^2 of 1.9 *versus* 9.9, compared with the ligand-free crystal structure scatter (*red line*). *D,* radius of gyration calculated from intensity during small angle X-ray scattering. The radius of gyration was calculated to be condensed when *N*-acetylmannosamine is bound (26.9 *versus* 27.5 Å), which is consistent with the inward shift represented by the crystal structure.

alize the lower catalytic rates with GlcNAc. The structure of GlcNAc–bound *Sa*NanK is similar to the *N*-acetylmannosamine–bound structure but appears to be slightly more open (Fig. S8), with an average RMSD for the four chains of 0.42 Å using 262–265 of the 285 residues (PyMOL). This alters the distances between catalytic residues Thr-11 and Thr-134, which provide electron stabilization to the β-phosphate of ATP and provides a possible explanation for lower catalytic rates with GlcNAc.

We then examined whether conformational change explains why the enzyme operates via an ordered or random kinetic mechanism. To do this we compared the ligand-free and sugar–bound structures of *Sa*NanK, which has a random ordered kinetic mechanism, with *S. griseus* glucokinase (PDB 3VGK and 3VGM), which has a compulsory-ordered kinetic mechanism, where glucose binds first and then ATP binds (16). Both *Sa*NanK and *S. griseus* glucokinase undergo a similar overall conformational shift, pivoting at the hinge region in response to sugar-binding and the ATP pocket is essentially unchanged (Fig. S9). Therefore, conformational change does not seem to explain why some ROK kinases have a random kinetic mechanism, whereas others have a compulsory-ordered kinetic mechanism.

To test whether the conformational change seen in the crystal structure also occurs in solution, small angle X-ray scattering was used. The scattering profile with and without *N*-acetylmannosamine were individually compared with the theoretical scatter of the crystal structures with and without *N*-acetylmannosamine using *CRYSOL* (33). The scattering data from the ligand-free *Sa*NanK sample closely matches the ligand-free *Sa*NanK crystal structure, but not the *N*-acetylmannosamine–bound crystal structure, (reduced χ^2 of 1.7 *versus* 4.9) (Fig. 4*B*). In contrast, the scattering data for *Sa*NanK in the presence of *N*-acetylmannosamine (5 mM) closely matches the *N*-acetylmannosamine–bound crystal structure, but not the ligand-free *Sa*NanK crystal structure (reduced χ^2 of 1.9 *versus* 9.9) (Fig. 5*C*). This demonstrates that the crystal structures match the solution structures and the enzyme closes around *N*-acetylmannosamine. The condensing of the *N*-acetylmannosamine solution structure is further supported by a smaller radius of gyration calculated from the overall scattering intensity (R_g = 26.9 *versus* 27.5 Å) (Fig. 5*D*).

To summarize, *Sa*NanK undergoes an *N*-acetylmannosamine–induced conformational change adopting a closed conformation. This ensures ATP hydrolysis only occurs in the presence of sugar substrate. In support, the catalytic residues (Asp-7, Thr-11, and Thr-134) that withdraw electrons from the β-phosphate group are only in an active configuration in the closed conformation. Adherence to the closed and open conformations, with and without ligand, respectively, is demonstrated in solution by small angle X-ray scattering.

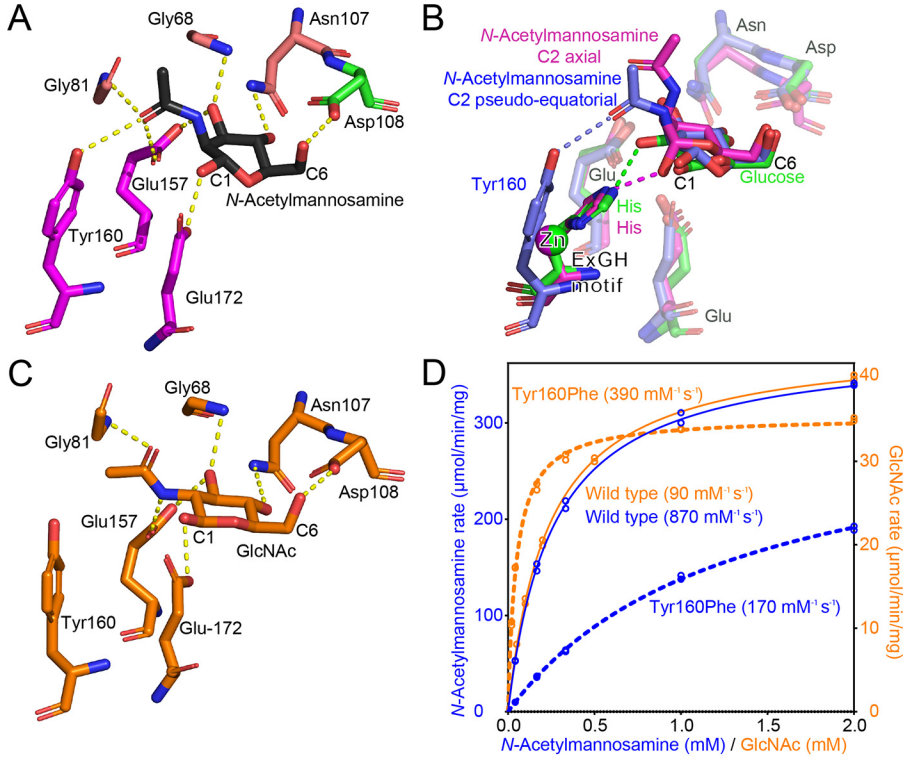

Figure 6. Involvement of *Sa*NanK Tyr-160 in substrate association. *A,* *N*-acetylmannosamine-bound *Sa*NanK. Gly-68, Asn-107, Asp-108, Glu-157, and Glu-172 bind the hydroxyl groups of *N*-acetylmannosamine and Gly-81, Glu-157, and Tyr-160 bind the C2 *N*-acetyl group. *B,* comparison of sugar substrate binding in *Sa*NanK (*blue*), *S. griseus* glucokinase (*green*), and human NanK (*pink*). In *Sa*NanK, the E*X*GH motif histidine is replaced by a tyrosine (Tyr-160), which binds the larger *N*-acetylated substrate by tilting backward from the active site and having greater length than histidine. In human NanK, the E*X*GH motif histidine bind the C1 hydroxyl and the axial *N*-acetyl group is bound by other nonconserved residues. *C,* GlcNAc bound *Sa*NanK. The *N*-acetyl carbonyl group is not able to hydrogen bond with Tyr-160. *D,* Tyr-160 provides substrate specificity toward *N*-acetylmannosamine, over GlcNAc. When tested with *N*-acetylmannosamine (*blue*, left axis), WT *Sa*NanK has more substrate specificity (870 mM^{-1} s^{-1}) than Y160F-substituted enzyme (170 mM^{-1} s^{-1}), which are absent the Tyr-160 hydroxyl. When tested with GlcNAc (*orange*, right axis), WT *Sa*NanK has less substrate specificity (90 mM^{-1} s^{-1}) than Y160F-substituted enzyme (390 mM^{-1} s^{-1}), demonstrating that Tyr-160 provides substrate specificity against GlcNAc.

The SaNanK active site uses tyrosine to bind the substrate C2 position

Five sugar substrate-binding residues are reported to be well-conserved in ROK kinases (13) and conservation was investigated in *Sa*NanK. Four of the five residues are conserved, including Asn-107, Asp-108, Glu-157, and Glu-172, whereas Tyr-160 is a nonconservative change and replaces the histidine in the canonical E*X*GH motif (discussed later). The C1 hydroxyl of *N*-acetylmannosamine is bound by Glu-172, and Glu-157 primarily binds C3, but also binds the C2 position *N*-acetyl moiety. Both residues are part of the larger $\alpha+\beta$ domain (Fig. 6*A*, *magenta*). Asn-107 binds the C4 hydroxyl and Asp-108 binds C6 (Fig. 6*A*). These residues border the N-terminal α/β domain and the hinge region, where the conserved substrate binding translates to the conformation change between the ligand–free and *N*-acetylmannosamine–bound structures. In addition to substrate binding, the conserved Asp-108 that binds the C6 position is also expected to feature in the catalytic mechanism by deprotonating the hydroxyl and increasing nucleophilicity (34). Consistent with the mechanism, Asp-108 is predicted to be deprotonated in the ligand–free structure (pK_a = 6.03), but protonated in the *N*-acetylmannosamine–bound structure (pK_a = 9.14), using *PDB2PQR* (35) at pH 7.

The structural role of Tyr-160 in the E*X*GY motif of *Sa*NanK is a nonconservative substitution of the Zn-binding histidine in the E*X*GH motif seen in canonical ROK kinases. Indeed, tyrosine at this position is conserved in other Gram-positive NanK lacking the Zn-binding motif (Fig. S1). The hydroxyl of *Sa*NanK Tyr-160 binds the C2 *N*-acetyl group of *N*-acetylmannosamine (Fig. 6*A*). This is analogous to ROK glucokinase, where the equivalent E*X*GH motif histidine binds the C2 hydroxyl of glucose (16). However, glucose is much smaller and the E*X*GH motif histidine also binds Zn. Zn-binding NanK enzymes utilize the E*X*GH motif histidine to bind the C1 hydroxyl and the larger *N*-acetyl substrate is bound from residues on the other side of the active site (31). A comparison of substrate binding is presented in Fig. 6*B*. In contrast to histidine found in the Zn-binding structures, *Sa*NanK Tyr-160 tilts away from the active site, increasing the size of the active site, and hydrogen bonds with the *N*-acetyl group. Interestingly, *N*-acetylmannosamine binds in a "boat" conformation and the *N*-acetyl group is in a pseudo-equatorial position (Fig. 6*B*, Figs. S10 and S11). It is unknown whether these observations are typical for NanK without the Zn-binding motif, although our sequence alignment suggests that tyrosine is consistently present at the position.

Our earlier kinetic analysis revealed that the C2 *N*-acetyl group is important for binding, with the K_m of both *N*-acetylmannosamine and GlcNAc (0.30 and 0.26 mM, respectively) being much lower than glucose (15 mM), which only differs at

Table 3
Kinetic parameters for *Sa*NanK substituted at Tyr-160

Without the Tyr-160 hydroxyl group, *Sa*NanK-Y160F and *Sa*NanK have a higher enzyme specificity (k_{cat}/K_m) with GlcNAc than for *N*-acetylmannosamine, the pathway substrate. The V_{max}, k_{cat}, and K_m were calculated in GraphPad Prism. The error is the mean ± S.E. of the fit. Values are apparent parameters, using saturating ATP concentration.

	N-Acetylmannosamine		GlcNAc	
	***Sa*NanK-Y160F**	***Sa*NanK-Y160A**	***Sa*NanK-Y160F**	***Sa*NanK-Y160A**
V_{max} (μmol/min/mg)	408 ± 5	422 ± 8	36.1 ± 0.3	33.6 ± 0.3
k_{cat} (s^{-1})	216 ± 3	223 ± 4	19.1 ± 0.2	17.8 ± 0.2
K_m (mM)	1.27 ± 0.1	1.34 ± 0.1	0.049 ± 0.002	0.057 ± 0.003
k_{cat}/K_m (s^{-1}/mM)	171 ± 13	167 ± 13	390 ± 16	310 ± 16

the C2 position. To investigate further, the GlcNAc–bound and *N*-acetylmannosamine–bound structures were compared. Both substrates are bound at the C1, C3, C4, and C6 hydroxyls by Glu-172, Glu-157, Gln-107, and Asp-108, respectively (Fig. 6, *A* and *C*). These positions are conserved with *S. griseus* glucokinase and glucose is expected to bind with *Sa*NanK in a similar manner. At the C2 position, the *N*-acetyl groups are both in an equatorial position, despite being enantiomers. *N*-Acetylmannosamine adopts a boat conformation with the carbonyl pointing "down" and the *N*-acetyl is positioned to bind three residues, Gly-81 to the carbonyl, Glu-157 to both the carbonyl and amine, and Tyr-160 to carbonyl (Fig. 6*A*). In contrast, GlcNAc adopts a "chair" conformation with carbonyl pointing "up" and the *N*-acetyl group is positioned to bind two residues only, Gly-81 to the carbonyl and Glu-157 to the amine (Fig. 6*C*). The comparison reveals that the *Sa*NanK active site is structurally optimized to bind *N*-acetylmannosamine, over GlcNAc and glucose.

Next, we tested the role of the Tyr-160 hydroxyl in substrate specificity by producing substituted enzyme *Sa*NanK-Y160F and comparing its kinetic profile (Table 3 and Fig. 6*D*). For *N*-acetylmannosamine, the specificity constant for the WT (k_{cat}/K_m = 870 mM^{-1} s^{-1}) is greater than the Y160F-substituted enzyme (k_{cat}/K_m = 170 mM^{-1} s^{-1}). This is consistent with the participation of the Tyr-160 hydroxyl in substrate binding for WT *Sa*NanK. For GlcNAc, the specificity constant for the WT (k_{cat}/K_m = 90 mM^{-1} s^{-1}) is lower than the Y160F-substituted enzyme (k_{cat}/K_m = 390 mM^{-1} s^{-1}). This suggests that the Tyr-160 hydroxyl may have a role in perturbing GlcNAc binding. In support of this, Tyr-160 is displaced by 1 Å, compared with the ligand–free and *N*-acetylmannosamine–bound structures, indicating that the residue sterically hinders GlcNAc binding. Together, the results demonstrate that the Tyr-160 hydroxyl is important for specificity toward the pathway substrate, with a 5:1 preference for *N*-acetylmannosamine with tyrosine, compared with a 2:1 preference for GlcNAc when replaced with phenylalanine. Controls with Y160A-substituted enzyme (Table 3) were similar to Y160F and further support that the tyrosine hydroxyl is important for *N*-acetylmannosamine specificity.

Without the Zn-bound E*X*GH motif histidine, *Sa*NanK binds the *N*-acetyl group of *N*-acetylmannosamine with tyrosine, which is generally conserved in Gram-positive NanK without the Zn-binding motif. This is different to Zn-binding NanK enzymes, which bind the *N*-acetyl group using residues on the other side of the active site (31). The tyrosine residue is important for substrate recognition and when replaced with phenylalanine, substrate preference shifts to GlcNAc.

The ROK Zn-binding motif is replaced by a stabilizing arginine stack

*Sa*NanK does not have the highly-conserved ROK Zn-binding motif, however, the significance of this is unknown as the purpose of the motif is not well-understood (13). To identify structural differences, *Sa*NanK was compared with a ROK and a non-ROK sugar kinase. In ROK *S. griseus* glucokinase, the Zn-binding region encompasses 20 residues, starting from the Zn-binding E*X*GH motif His-157 to the end of the motif, C*X*CG*XX*GC*X*(E/D) (residues 167–176, PDB 3VGK). The E*X*GH motif histidine and the Zn-motif Glu/Asp bind to the sugar, with the central residues forming a loop that wraps around Zn (Fig. 1*C*) enclosing the active site (Fig. 7*A*, *green*). For *Sa*NanK ROK without the Zn-motif, the equivalent region between the sugar-binding Tyr-160 and Glu-172 (13 residues) forms a loop that associates with the large α+β domain and does not occlude the sugar active site (Fig. 7*A*, *red*). In non-ROK *E. coli* glucokinase, the equivalent region is 28 residues long (His-160–Glu-187) and features highly charged residues as part of the dimerization interface (14). This does not occlude the sugar active site (Fig. 7*A*, *yellow*) in a position similar to the *Sa*NanK region. The observations suggest that the absence of Zn-binding corresponds with an open sugar active site and the presence of Zn-binding corresponds with a closed active site.

The absence or presence of the Zn-motif may determine the order of substrate binding. We propose that *Sa*NanK has a random-order kinetic model because the absence of the Zn-motif provides a secondary substrate entry point, whereas in the compulsory-order *S. griseus* glucokinase there is a narrow active site with a just a single entry and glucose must access the pocket at the bottom before ATP binds. Kinetics assays demonstrate that *Sa*NanK uses a random-order ternary complex for catalysis, whereas canonical ROK *S. griseus* glucokinase is characterized as a compulsory-ordered complex that requires glucose to bind before ATP (16). Initially, conformational change was investigated as a method of conferring order (discussed above), but comparisons of the enzyme structures failed to identify a differentiating feature in ATP-binding site and it is difficult to attribute the difference in mechanism to conformational change. Compulsory-ordered *S. griseus* glucokinase has a narrow active site with a single opening near the ATP-binding pocket (Fig. 7*A*). Glucose binds at the bottom of the active site and ATP binding would obstruct glucose binding, thus providing an explanation of why glucose must bind before ATP. In contrast, *Sa*NanK has a secondary opening near the active site that *N*-acetylmannosamine can access irrespective of ATP binding providing for a random-ordered kinetic mechanism.

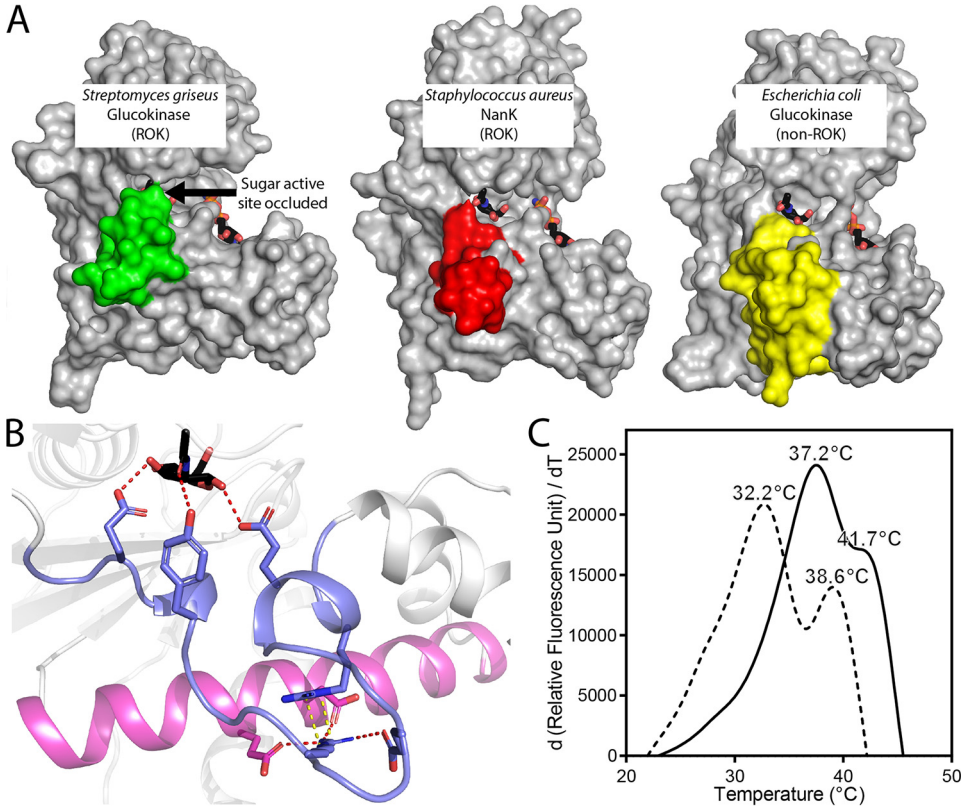

Figure 7. Arginine stacking feature in the region equivalent to the ROK Zn-binding motif. *A,* comparison of region equivalent to the ROK Zn-binding motif. In non-Zn–binding ligand-free *Sa*NanK (*red*) the region is positioned away from the sugar active site. In Zn-binding ROK *S. griseus* glucokinase (PDB 3VGK) (*green*) the region partially covers the sugar active site. Glucokinase family *E. coli* glucokinase (PDB 1Q18) (*yellow*) has a larger region featuring an α-helix and is positioned away from the sugar active site. *N*-Acetylmannosamine and ATP substrates were aligned from *N*-acetylmannosamine–bound *Sa*NanK and ROK kinase (PDB 3VGL). *B,* in the region equivalent to the Zn-binding motif (*blue*), *Sa*NanK features a π-stacking arginine pair, which are coordinated by three negative residues. Two of the negative residues are part of a large α-helix (*pink*) stabilizing the protein loop and positioning it away from the active site. Stable positioning of the region is important as it features three active site residues (Glu-157, Tyr-160, and Glu-172), which bind to *N*-acetylmannosamine (*black*). *C,* differential scanning fluorimetry with *Sa*NanK (*solid line*) and *Sa*NanK-R164K (*dashed line*). *Sa*NanK-R164K has lower thermal stability with the average melting temperature of the two domains is 4.1 °C lower than WT.

ROK Zn-binding has been demonstrated elsewhere to be necessary for activity (15, 18), and Zn coordination is hypothesized to organize three nearby active site residues (16). The organization of equivalent residues (Glu-157, Tyr-160, and Glu-172) were examined in *Sa*NanK to investigate why the enzyme is active without Zn-binding. Glu-157, Tyr-160, and Glu-172 are well-organized in the ligand-free structure with lower B-factors (17.5, 13.8, and 18.8) than the model average (37.7), despite little secondary structure organization in the region. The nearby region, equivalent to the ROK Zn-binding region, was examined for potential stabilizing features. Interestingly, the region features two stacked arginine residues (Arg-164 and Arg-174), ionically coordinated by three negatively charged residues (Glu-167, Asp-219, and Glu-222), with two of the negative residues belonging to a large α-helix that anchors the arginine stack (Fig. 7*B*). Potentially, this five-coordinate feature stabilizes the region and organizes the active site residues, serving the hypothesized role of four-coordinate Zn-binding in canonical ROK.

Re-examination of Gram-positive NanK sequence alignments reveals that the arginine stacking residues are novel within the *Staphylococcus* genus and Arg-164, which is coordinated by four other residues, is not conserved elsewhere (Fig. S12). Arg-164 was substituted with alanine and we test the effect of this change on thermal stability to test for structural stabilization, and kinetic assays to test whether the residue is important for active site organization (a hypothesized role of the equivalent Zn-binding region (16)). *Sa*NanK-R164A was not recoverable in the soluble fraction and attempts to improve solubility by altering the expression temperature and length were unsuccessful. This suggests the enzyme is potentially unstable without the positive charge or hydrophobic stacking supplied by arginine. However, *Sa*NanK-R164K was successfully purified. Thermal stability analysis reveals that *Sa*NanK-R164K has an average T_m of 35.4 °C, which is 4.1 °C lower than *Sa*NanK (Fig. 7*C*), and in conjunction with insolubility of *Sa*NanK-R164A, this indicates that arginine interaction is important for stabilization. Kinetic assays show that the substituted enzyme is catalytically compromised (V_{max} = 6.1 ± 0.3 μmol/min/mg, k_{cat} = 3.2 ± 0.2 s^{-1}, K_m = 0.26 ± 0.01 mM) with approximately a 100-fold decrease in activity compared with WT (k_{cat} = 262.6 s^{-1}). This is consistent with arginine stacking contributing to organize the nearby active site residues. This is a hypothesized role of the ROK Zn-binding region, which is equivalently positioned to the *Sa*NanK arginine stack, and we propose that both coordinating features provide stabilization and organization.

The absence of the Zn-binding motif increases the potential of *Sa*NanK as a drug target. Elsewhere, it has been demonstrated that the bacterial sialic acid catabolic pathway is a viable target to lower infectivity and increase antibiotic efficacy (1, 3, 4, 9, 10). Targeting the pathway is only useful if toxic interaction with host sialic pathway enzymes can be avoided. The NanK component of human bifunctional UDP-GlcNAc 2-epimerase/*N*-acetylmannosamine kinase is a ROK family protein but, unlike *Sa*NanK, it retains the canonical Zn-binding motif (31). The structure of the human enzyme (PDB 2YHY) shows that bound *N*-acetylmannosamine is enclosed by the Zn-binding motif and the *N*-acetyl group associates in the axial position. Whereas, our characterization demonstrates that *Sa*NanK is open at the *N*-acetylmannosamine end of the active site (Fig. 7*A*). Therefore, we propose that synthesized glucose or mannose C2 (or C1) derivatives can be made to target *Sa*NanK and not the human bifunctional enzyme, where the Zn-binding motif occludes larger derivative.

Conclusions

Gram-positive NanK enzymes are annotated as ROK enzymes, but many are missing the identifying ROK Zn-binding motif and have tyrosine in place of the histidine in the E*X*GH motif. Here we investigate the effect of these changes on the structure and function of *Sa*NanK. We focus on defining the role of tyrosine that replaces E*X*GH motif histidine and provide insight into the presence or absence of Zn in ROK kinases.

We report the first functional and structural study of a Gram-positive NanK. The crystal and solution structures conform to the RNase H-like–fold present in ROK family proteins (36) and we confirm that the enzyme is catalytically active as a kinase. Therefore, *Sa*NanK has the properties expected from a ROK kinase. Investigation of the protein dynamics reveal the structure condenses with sugar substrate in the X-ray crystal form, as reported for other ROK kinases (16, 31). For the first time, we confirm this in solution with small-angle X-ray scattering experiments.

Our sequence alignment reports that Gram-positive NanK without the Zn-binding motif have tyrosine in place of E*X*GH motif histidine. Structural and functional analysis reveals that tyrosine binds C2 *N*-acetyl of *N*-acetylmannosamine by tilting backward from the active site. This is substantially different from Zn-binding NanK, where the E*X*GH motif histidine binds C1 and is restrained in a forward-facing tilt by secondary binding of Zn. As E*X*GH motif histidine binds Zn, the use of tyrosine in Gram-positive NanK is certainly linked to the loss of Zn-binding. However, as Gram-positive NanK are highly divergent at a sequence level, it is difficult to know whether change of histidine from the E*X*GH motif or Zn-binding motif residues occurred first.

The role of the Zn-binding motif is not well-understood, therefore the significance of its absence in Gram-positive NanK is unknown. Our examination considered the absence of Zn-binding in *Sa*NanK and its presence in canonical ROK. A role hypothesized for Zn-binding is that it organizes the active site residues for catalysis (16). We find a possibly equivalent coordinating feature in *Sa*NanK: an arginine stack that is novel to *Staphylococcus*. Loss of this feature in *Sa*NanK lowered thermal stability and significantly lowered catalytic rates, consistent with the hypothesis that it is a feature that provides structural stabilization and active site coordination, as opposed to being provided by that Zn-binding in other ROK kinases. Our structural comparison also revealed that absence of the motif provides an opening at the sugar substrate active site. This is beneficial for the active site access of larger substrates, such as *N*-acetylmannosamine in *Sa*NanK and potentially, disaccharide cellobiose kinases (23). Whereas Zn-binding in *E. coli* NanK requires increased hinge flexibility for *N*-acetylmannosamine association (19). We propose that the ROK Zn-binding motif is an adaptation that excludes large substrates, consistent with ROK repressors and kinases generally functioning with small sugars (13) that may also contribute to compulsory-ordered catalysis for pathway regulation (16, 24). Finally, given the proximity of the arginine stack and E*X*GY motif, we propose that this is a unique substructure to target with inhibitory compounds that avoid off-target effects with the human homologue, bifunctional NanK.

Experimental procedures

Bioinformatics

To provide a root for the phylogenetic tree of NanK protein sequences, sequences for glucokinase, fructokinase, and GlcNAc kinase enzymes that were closely related to the canonical ROK sequence were added to the alignment. To select the root sequences, the ROK Hidden Markov Model (HMM) sequence from the Pfam database (https://pfam.xfam.org/family/PF00480/hmm)[4] was entered into pBLAST (https://blast.ncbi.nlm.nih.gov/Blast.cgi), alongside the search terms "glucokinase," "fructokinase," or "GlcNAc kinase." The top three sequence results (from unique genera) were included in the alignment. NanK protein sequences were searched for by inputting the *Sa*NanK sequence, ROK HMM sequence, and *E. coli* NanK sequence, alongside the search term "*N*-acetylmannosamine kinase" into the tBLASTn database. The first NanK sequence for each unique genus were added to the alignment. Additionally, sequences that had a different variation of E*X*GH motif or Zn-binding residues, were included. To verify sequences were annotated correctly, only sequences clustered with Nan genes were included.

Cloning, expression, and purification

*Sa*NanK-R164A, -R164K, and -Y160A were constructed by Genscript based on variation of the *Sa*NanK (accession number YP_498886.1) codon optimized for expression in *E. coli*. *Sa*NanK-R164A was synthesized *de novo* and inserted into a pET30ΔSE plasmid between NdeI and HindIII restriction sites. *Sa*NanK-R164K was then created by site-directed mutagenesis.

*Sa*NanK-Y160F was obtained by in-house site-directed mutagenesis of the pET30ΔSE-*Sa*NanK (17, 37) using the infu-

[4] Please note that the JBC is not responsible for the long-term archiving and maintenance of this site or any other third party hosted site.

sion protocol (38), with forward primer (5′-A GTT GGG TTT TTA TTG TAT CGT CCA ACT GAA AA-3′) and reverse primer (5′-AA TAA AAA CCC AAC TTC ATT TGC CTT ATG A-3′). Constructs were verified through DNA sequencing by Macrogen (Korea).

The protocol for expression and purification of WT protein has previously been reported (17). Briefly, *E. coli* BL21 (DE3) cells were transformed with pET30ΔSE/NanK, then cultured in Luria-Broth containing kanamycin (30 μg ml^{-1}) at 37 °C, 180 rpm until an OD_{600} of 0.6 was reached. Expression was induced with isopropyl β-D-1-thiogalactopyranoside at a final concentration of 1 mM and incubated overnight at 26 °C. Purification was conducted at 4 °C. Cells were harvested at 6,000 × *g* for 10 min using a Thermo Sorvall RC-6-Plus centrifuge and resuspended in 20 mM Tris-HCl, pH 8.0. The cells were lysed for 10 min (Hielscher UP200S Ultrasonic Processor at 70%, 0.5 s on/off cycle) and lysate containing soluble protein was extracted from the supernatant after centrifugation at 24,000 × *g*. For anion exchange chromatography, the sample was applied to a 20-ml Q-Sepharose anion exchange column (GE Healthcare) pre-equilibrated with lysis buffer, then eluted with an increasing concentration gradient of 20 mM Tris-HCl, pH 8.0, 1 M NaCl. For hydrophobic exchange chromatography, ammonium sulfate was added to the eluted protein to a final concentration of 1 M and applied to a 20-ml Phenyl-Sepharose FF column (GE Healthcare) pre-equilibrated with 20 mM Tris-HCl, pH 8.0, 1 M ammonium sulfate and eluted using an increasing concentration gradient of 20 mM Tris-HCl, pH 8.0. Finally, size exclusion chromatography was conducted with a HiLoad 16/60 Superdex 200 column (GE Healthcare) using 20 mM Tris-HCl, pH 8.5. Final purity was estimated using SDS-PAGE gels (Fig. S13). Exceptions to this procedure were as follows; selenomethionine-substituted protein was produced using PASM-5052 autoinduction media (39) and expression trials of R164A mutants were conducted at 20 and 26 °C, for 4, 8, and 16 h.

Enzyme kinetics

Initial rate data were recorded using a pyruvate kinase/lactate dehydrogenase-coupled assay (19). NADH oxidation was monitored using a CARY 100 Bio UV-visible spectrophotometer (Agilent Technologies) based on an extinction coefficient of 6220 M^{-1} cm^{-1} at 340 nm (40). The reaction mixture incubated for 15 min at 25 °C consisted of a pyruvate kinase/lactate dehydrogenase mixture (10 μl, purchased from Sigma SKU-P0294), purified WT *Sa*NanK, 0.017 mg ml^{-1}, 536 nM (10 μl), 50 mM phosphoenolpyruvate (20 μl), 8 mM NADH (20 μl), ATP varied concentration (20 μl), and kinetics buffer, 22 mM Tris-HCl, pH 8.5, 20 mM KCl, 5 mM $MgCl_2$ (900 μl), listed values are initial concentrations. The reaction was initiated with sugar substrate (20 μl, at varied concentration), which was also incubated at 25 °C. To ensure that the *N*-acetylmannosamine kinase concentration was directly proportional with the rate, it was checked that the coupling enzymes were in excess and that there was no background reaction. The enzyme appeared to be less stable when incubated at 30 °C or above, which was consistent with a differential scanning fluorimetry experiment demonstrating that the melting temperature of *Sa*NanK is 39.5 °C (Fig. 7*C*). Moreover, the enzyme was deactivated when in Tris-HCl buffer at pH 8 or below. The data were processed using GraphPad Prism 6.0 (GraphPad Software, La Jolla, CA). The model that best fitted the data (ternary complex (Equation 1) or substituted complex models (Equation 2)) was determined by evaluating the AICc values (41) (ternary complex = 129.8, substituted complex = 203.4). Single substrate (apparent) kinetic parameters were determined using the Michaelis-Menten model.

Initial rate equations for ternary and substituted complexes (42) are shown.

$$v = \frac{v_{ab}}{K_{iA}K_{mB} + K_{mB}a + K_{mA}b + ab} \quad \text{(Eq. 1)}$$

$$v = \frac{v_{ab}}{K_{mB}a + K_{mA}b + ab} \quad \text{(Eq. 2)}$$

Analytical ultracentrifugation

Analytical ultracentrifugation was performed using an XL-I analytical ultracentrifuge (Beckman Coulter) at 50,000 rpm at 20 °C. Sedimentation velocity experiments were conducted with *N*-acetylmannosamine kinase at 0.3, 0.6, and 0.9 mg ml^{-1} (9.5, 18.9, and 28.4 μM), in 20 mM Tris-HCl, pH 8.5, 100 mM KCl. Sample (380 μl) and reference buffer (400 μl) were loaded into 12-mm double-sector quartz cells with standard Epon 2-channel centerpieces and mounted in an An-50 Ti 8-hole rotor (Beckman). Radial absorbance was measured at 280 nm with a step size of 0.003 cm over 80 scans. *SEDNTERP* software was used to calculate values for solvent density and solvent viscosity and to estimate partial specific volume, based on the amino acid sequence (43). *SEDFIT* was then used to fit the data with continuous size distribution ($c(s)$) and continuous mass distribution ($c(M)$) models (28). Residuals were examined to review that noise was normally distributed and data points were checked for fit with curves (Fig. S4).

Small angle X-ray scattering

Small angle X-ray scattering was undertaken at the Australian Synchrotron on the SAXS/WAXS beamline equipped with a PILATUS 1M detector (170 × 170 mm, effective pixel size 172 × 172 μm), as described by Griffin *et al.* (44). The X-ray wavelength provided was 1.0332 Å and the sample detector distance was set at 1600 mm, which produced a q range of 0.006 – 0.4 Å^{-1}. *Sa*NanK (6 mg ml^{-1}, 189 μM, 50 μl) was injected onto an inline Superdex 200 5/150 GL (GE Healthcare) using a co-flow setup (61). The column was equilibrated with 20 mM Tris-HCl, pH 8.0, 100 mM NaCl and the radical scavengers, 5% (v/v) glycerol and 0.1% (w/v) sodium azide, using a flow rate of 0.45 ml min^{-1}. Additionally, 5 mM *N*-acetylmannosamine was added to the equilibration buffer above for the sugar-bound sample. Over the course of the elution, scattering data were collected in 1-s exposures using a 1.0-mm glass capillary at 12 °C.

To process the scattering data, *ScatterBrain IDL* (version 2.822, Australian Synchrotron Facility) was employed for initial data reduction, radial integration of individual frames, and the

conversion of 1D data files. Data were buffer-subtracted using *CHROMIXS* (45). The *ATSAS* software suite (version 2.8.0) was used for all further analysis (29), including calculation of the radius of gyration and pairwise distribution functions *P*(r). Theoretical scattering of the *Sa*NanK crystal structures were calculated using *CRYSOL* (33).

X-ray crystallography

Crystallization was performed using the sitting-drop vapor-diffusion method at 20 °C. For selenomethioinine-substituted SaNanK, drops were composed of 10 mg ml^{-1} of enzyme (200 nl) and reservoir solution (200 nl) containing 0.2 M sodium malonate dibasic monohydrate, 20% (w/v) PEG 3350 (Molecular Dimensions, PACT *premier* HT-96 Screen, condition E12). For *N*-acetylmannosamine– and GlcNAc–bound enzyme, drops contained *Sa*NanK 10 mg ml^{-1} and either *N*-acetylmannosamine or GlcNAc 10 mM (200 nl), plus a reservoir solution of 0.2 M L-arginine, 0.1 M sodium acetate, pH 5.0, in 8% (w/v) poly-γ-glutamic acid (200 nl) (Molecular Dimensions, PGA HT-96 Screen, condition A8). The crystals were cryo-protected by soaking in 15% ethylene glycol solution and reservoir solution prior to freezing in liquid nitrogen.

The Australian Synchrotron MX1 and MX2 beamlines were used for data collection. Data collected for the selenomethionine-substituted enzyme was processed using *iMosflm* (46) and *AIMLESS* (47). For enzyme with *N*-acetylmannosamine and GlcNAc, data were processed with *XDS* and *AIMLESS* (47). X-ray diffraction parameters are reported in Table 2.

Experimental phasing was conducted using anomalous scattering of *Sa*NanK from selenium-derivatized methionine (6 sites per monomer). The diffraction data were phased using single anomalous diffraction processed by *SHELXC/D/E*, including automated model building (26). Electron density of the final resolved phases are demonstrated in Fig. S3. Phases of *N*-acetylmannosamine– and GlcNAc–bound *Sa*NanK were calculated using the ligand-free *Sa*NanK structure as a molecular replacement model with *MOLREP* (48). Models were iteratively refined and built, using *REFMAC5* and *COOT* (49, 50). Finalization and model validation was conducted using *phenix.refine* and *MOLPROBITY* (51, 52).

Attempts to solve the phases of ligand-free nonselenomethionine-substituted *Sa*NanK using molecular replacement were unsuccessful. Search models for *Sa*NanK were selected based on the highest sequence identity: 2GUP, 3VOV, 3VGK, and 4HTL (identity = 28.0–24.6%). Additionally, two NanK structures were also trialled, PDB 2YHY and 2AA4 (identity = 21.9–21.4%). The models were split into monomeric units and processed with *CHAINSAW*, to generate the search model, and molecular replacement was attempted using *MOLREP* and *PHASER* (48, 53). We also tried partial models and lower packing restraints (54), but these were also unsuccessful.

Author contributions—D. C., R. A. N., and R. C. D. conceptualization; D. C., S. P., and M. D. G. formal analysis; D. C., J. S. D., M. C. N.-V., C. R. H., and R. A. N. investigation; D. C. and R. A. N. methodology; D. C. writing-original draft; D. C., J. S. D., C. R. H., T. G. S., R. S., J. W. B. M., R. F., S. P., M. D. G., R. A. N., and R. C. D. writing-review and editing; R. A. N. and R. C. D. supervision.

Acknowledgments—Parts of this research were conducted at the SAXS/WAXS and MX2 beamlines of the Australian Synchrotron and the Australian Nuclear Science and Technology Organization, and made use of the ACRF Detector at the MX2 beamline. Initial crystallization screens were conducted at the CSIRO Collaborative Crystallization Centre (www.csiro.au/C3),[4] Melbourne, Australia.

References

1. Severi, E., Hood, D. W., and Thomas, G. H. (2007) Sialic acid utilization by bacterial pathogens. *Microbiology* **153,** 2817–2822 CrossRef Medline
2. von Itzstein, M. (2007) The war against influenza: discovery and development of sialidase inhibitors. *Nat. Rev. Drug Discov.* **6,** 967–974 CrossRef Medline
3. Vimr, E. R., and Troy, F. A. (1985) Identification of an inducible catabolic system for sialic acids (nan) in *Escherichia coli*. *J. Bacteriol.* **164,** 845–853 Medline
4. Komatsuzawa, H., Fujiwara, T., Nishi, H., Yamada, S., Ohara, M., McCallum, N., Berger-Bächi, B., and Sugai, M. (2004) The gate controlling cell wall synthesis in *Staphylococcus aureus*. *Mol. Microbiol.* **53,** 1221–1231 CrossRef Medline
5. Perez-Vilar, J., and Hill, R. L. (1999) The structure and assembly of secreted mucins. *J. Biol. Chem.* **274,** 31751–31754 CrossRef Medline
6. North, R. A., Wahlgren, W. Y., Remus, D. M., Scalise, M., Kessans, S. A., Dunevall, E., Claesson, E., Soares da Costa, T. P., Perugini, M. A., Ramaswamy, S., Allison, J. R., Indiveri, C., Friemann, R., and Dobson, R. C. J. (2018) The sodium sialic acid symporter from *Staphylococcus aureus* has altered substrate specificity. *Front. Chem.* **6,** 233–233 CrossRef Medline
7. North, R. A., Horne, C. R., Davies, J. S., Remus, D. M., Muscroft-Taylor, A. C., Goyal, P., Wahlgren, W. Y., Ramaswamy, S., Friemann, R., and Dobson, R. C. J. (2018) "Just a spoonful of sugar": import of sialic acid across bacterial cell membranes. *Biophys. Rev.* **10,** 219–227 CrossRef Medline
8. Wahlgren, W. Y., Dunevall, E., North, R. A., Paz, A., Scalise, M., Bisignano, P., Bengtsson-Palme, J., Goyal, P., Claesson, E., Caing-Carlsson, R., Andersson, R., Beis, K., Nilsson, U. J., Farewell, A., Pochini, L., *et al.* (2018) Substrate-bound outward-open structure of a Na^+-coupled sialic acid symporter reveals a new Na^+ site. *Nat. Commun.* **9,** 1753 CrossRef Medline
9. Almagro-Moreno, S., and Boyd, E. F. (2009) Sialic acid catabolism confers a competitive advantage to pathogenic *Vibrio cholerae* in the mouse intestine. *Infect. Immun.* **77,** 3807–3816 CrossRef Medline
10. Olson, M. E., King, J. M., Yahr, T. L., and Horswill, A. R. (2013) Sialic acid catabolism in *Staphylococcus aureus*. *J. Bacteriol.* **195,** 1779–1788 Medline
11. Coombes, D., Moir, J. W. B., Poole, A. M., Cooper, T. F., and Dobson, R. C. J. (2019) The fitness challenge of studying molecular adaptation. *Biochem. Soc. Trans.* **47,** 1533–1542 CrossRef Medline
12. Davies, J. S., Coombes, D., Horne, C. R., Pearce, F. G., Friemann, R., North, R. A., and Dobson, R. C. J. (2019) Functional and solution structure studies of amino sugar deacetylase and deaminase enzymes from *Staphylococcus aureus*. *FEBS Lett.* **593,** 52–66 CrossRef
13. Conejo, M. S., Thompson, S. M., and Miller, B. G. (2010) Evolutionary bases of carbohydrate recognition and substrate discrimination in the ROK protein family. *J. Mol. Evol.* **70,** 545–556 CrossRef Medline
14. Lunin, V. V., Li, Y., Schrag, J. D., Iannuzzi, P., Cygler, M., and Matte, A. (2004) Crystal structures of *Escherichia coli* ATP-dependent glucokinase and its complex with glucose. *J. Bacteriol.* **186,** 6915–6927 CrossRef Medline
15. Mesak, L. R., Mesak, F. M., and Dahl, M. K. (2004) Bacillus subtilis GlcK activity requires cysteines within a motif that discriminates microbial glucokinases into two lineages. *BMC Microbiol.* **4,** 6 CrossRef Medline
16. Miyazono K., Tabei, N., Morita, S., Ohnishi, Y., Horinouchi, S., and Tanokura, M. (2012) Substrate recognition mechanism and substrate-dependent conformational changes of an ROK family glucokinase from *Streptomyces griseus*. *J. Bacteriol.* **194,** 607–616 CrossRef Medline

17. North, R. A., Seizova, S., Stampfli, A., Kessans, S. A., Suzuki, H., Griffin, M. D., Kvansakul, M., and Dobson, R. C. (2014) Cloning, expression, purification, crystallization and preliminary X-ray diffraction analysis of *N*-acetylmannosamine kinase from methicillin-resistant *Staphylococcus aureus*. *Acta Crystallogr. F Struct. Biol. Commun.* **70,** 643–649 CrossRef
18. Schiefner, A., Gerber, K., Seitz, S., Welte, W., Diederichs, K., and Boos, W. (2005) The crystal structure of Mlc, a global regulator of sugar metabolism in *Escherichia coli*. *J. Biol. Chem.* **280,** 29073–29079 Medline
19. Larion, M., Moore, L. B., Thompson, S. M., and Miller, B. G. (2007) Divergent evolution of function in the ROK sugar kinase superfamily: role of enzyme loops in substrate specificity. *Biochemistry* **46,** 13564–13572 CrossRef Medline
20. Vergne-Vaxelaire, C., Mariage, A., Petit, J.-L., Fossey-Jouenne, A., Guérard-Hélaine, C., Darii, E., Debard, A., Nepert, S., Pellouin, V., Lemaire, M., Zaparucha, A., Salanoubat, M., and de Berardinis, V. (2018) Characterization of a thermotolerant ROK-type mannofructokinase from *Streptococcus mitis*: application to the synthesis of phosphorylated sugars. *Appl. Microbiol. Biotechnol.* **102,** 5569–5583 CrossRef Medline
21. Skarlatos, P., and Dahl, M. K. (1998) The glucose kinase of *Bacillus subtilis*. *J. Bacteriol.* **180,** 3222–3226 CrossRef Medline
22. Uehara, T., and Park, J. T. (2004) The *N*-acetyl-D-glucosamine kinase of *Escherichia coli* and its role in murein recycling. *J. Bacteriol.* **186,** 7273–7279 CrossRef Medline
23. Thompson, J., Lichtenthaler, F. W., Peters, S., and Pikis, A. (2002) β-Glucoside Kinase (BglK) from *Klebsiella pneumoniae*: purification, properties, and preparative synthesis of 6-phospho-β-D-glucosides. *J. Biol. Chem.* **277,** 34310–34321 CrossRef Medline
24. Imriskova, I., Arreguín-Espinosa, R., Guzmán, S., Rodriguez-Sanoja, R., Langley, E., and Sanchez, S. (2005) Biochemical characterization of the glucose kinase from *Streptomyces coelicolor* compared to *Streptomyces peucetius* var. caesius. *Res. Microbiol.* **156,** 361–366 CrossRef Medline
25. Ringborg, R. H., and Woodley, J. (2016) The application of reaction engineering to biocatalysis. *React. Chem. Eng.* **1,** 10–22 CrossRef
26. Sheldrick, G. (2008) A short history of SHELX. *Acta Crystallogr. A* **64,** 112–122 CrossRef Medline
27. Zhang, Y., and Skolnick, J. (2005) TM-align: a protein structure alignment algorithm based on the TM-score. *Nucleic Acids Res.* **33,** 2302–2309 CrossRef Medline
28. Schuck, P. (2000) Size-distribution analysis of macromolecules by sedimentation velocity ultracentrifugation and lamm equation modeling. *Biophys. J.* **78,** 1606–1619 CrossRef Medline
29. Petoukhov, M. V., Franke, D., Shkumatov, A. V., Tria, G., Kikhney, A. G., Gajda, M., Gorba, C., Mertens, H. D., Konarev, P. V., and Svergun, D. I. (2012) New developments in the ATSAS program package for small-angle scattering data analysis. *J. Appl. Crystallogr.* **45,** 342–350 CrossRef Medline
30. Krissinel, E., and Henrick, K. (2007) Protein interfaces, surfaces and assemblies service PISA at European Bioinformatics Institute. *J. Mol. Biol.* **372,** 774–797 CrossRef Medline
31. Martinez, J., Nguyen, L. D., Hinderlich, S., Zimmer, R., Tauberger, E., Reutter, W., Saenger, W., Fan, H., and Moniot, S. (2012) Crystal structures of *N*-acetylmannosamine kinase provide insights into enzyme activity and inhibition. *J. Biol. Chem.* **287,** 13656–13665 CrossRef Medline
32. Caing-Carlsson, R., Goyal, P., Sharma, A., Ghosh, S., Setty, T. G., North, R. A., Friemann, R., and Ramaswamy, S. (2017) Crystal structure of *N*-acetylmannosamine kinase from *Fusobacterium nucleatum*. *Acta Crystallogr. F Struct. Biol. Commun.* **73,** 356–362 CrossRef
33. Svergun, D., Barberato, C., and Koch, M. H. (1995) CRYSOL: a program to evaluate X-ray solution scattering of biological macromolecules from atomic coordinates. *J. Appl. Crystallogr.* **28,** 768–773 CrossRef
34. Nocek, B., Stein, A. J., Jedrzejczak, R., Cuff, M. E., Li, H., Volkart, L., and Joachimiak, A. (2011) Structural studies of ROK fructokinase YdhR from *Bacillus subtilis*: insights into substrate binding and fructose specificity. *J. Mol. Biol.* **406,** 325–342 CrossRef Medline
35. Jurrus, E., Engel, D., Star, K., Monson, K., Brandi, J., Felberg, L. E., Brookes, D. H., Wilson, L., Chen, J., Liles, K., Chun, M., Li, P., Gohara, D. W., Dolinsky, T., Konecny, R., *et al*. (2018) Improvements to the APBS biomolecular solvation software suite. *Protein Sci.* **27,** 112–128 CrossRef Medline
36. Murzin, A. G., Brenner, S. E., Hubbard, T., and Chothia, C. (1995) SCOP: a structural classification of proteins database for the investigation of sequences and structures. *J. Mol. Biol.* **247,** 536–540 CrossRef Medline
37. Suzuki, H., Tabata, K., Morita, E., Kawasaki, M., Kato, R., Dobson, R. C., Yoshimori, T., and Wakatsuki, S. (2014) Structural basis of the autophagy-related LC3/Atg13 LIR complex: recognition and interaction mechanism. *Structure* **22,** 47–58 CrossRef Medline
38. Zhu, B., Cai, G., Hall, E. O., and Freeman, G. J. (2007) In-Fusion™ assembly: seamless engineering of multidomain fusion proteins, modular vectors, and mutations. *BioTechniques* **43,** 354–359 CrossRef Medline
39. Sreenath, H. K., Bingman, C. A., Buchan, B. W., Seder, K. D., Burns, B. T., Geetha, H. V., Jeon, W. B., Vojtik, F. C., Aceti, D. J., Frederick, R. O., Phillips, G. N., Jr., and Fox, B. G. (2005) Protocols for production of selenomethionine-labeled proteins in 2-L polyethylene terephthalate bottles using auto-induction medium. *Protein Expr. Purif.* **40,** 256–267 CrossRef Medline
40. Horecker, B. L., and Kornberg, A. (1948) The extinction coefficients of the reduced band of pyridine nucleotides. *J. Biol. Chem.* **175,** 385–390 Medline
41. Kakkar, T., Pak, Y., and Mayersohn, M. (2000) Evaluation of a minimal experimental design for determination of enzyme kinetic parameters and inhibition mechanism. *J. Pharmacol. Exp. Ther.* **293,** 861–869 Medline
42. Cornish-Bowden, A. (1995) Reactions of more than one substrate. in *Fundamentals of Enzyme Kinetics*, pp. 129–158, Portland Press Ltd., London
43. Laue, T., Shah, B., Ridgeway, T., and Pelletier, S. (1992) Computer-aided interpretation of analytical sedimentation data for proteins. in *Analytical Ultracentrifugation in Biochemistry and Polymer Science* (Harding, S., Rowe, A., and Horton, J., eds) pp. 90–125, Royal Society of Chemistry, Cambridge
44. Griffin, M. D. W., Billakanti, J. M., Wason, A., Keller, S., Mertens, H. D. T., Atkinson, S. C., Dobson, R. C. J., Perugini, M. A., Gerrard, J. A., and Pearce, F. G. (2012) Characterization of the first enzymes committed to lysine biosynthesis in *Arabidopsis thaliana*. *PLoS ONE* **7,** e40318-e40318 CrossRef
45. Panjkovich, A., and Svergun, D. I. (2018) CHROMIXS: automatic and interactive analysis of chromatography-coupled small-angle X-ray scattering data. *Bioinformatics* **34,** 1944–1946 CrossRef Medline
46. Battye, T. G., Kontogiannis, L., Johnson, O., Powell, H. R., and Leslie, A. G. (2011) iMOSFLM: a new graphical interface for diffraction-image processing with MOSFLM. *Acta Crystallogr. D Biol. Crystallogr.* **67,** 271–281 CrossRef Medline
47. Evans, P. R., and Murshudov, G. N. (2013) How good are my data and what is the resolution? *Acta Crystallogr. D Biol. Crystallogr.* **69,** 1204–1214 CrossRef Medline
48. Vagin, A., and Teplyakov, A. (2010) Molecular replacement with MOLREP. *Acta Crystallogr. D Biol. Crystallogr.* **66,** 22–25 CrossRef Medline
49. Emsley, P., Lohkamp, B., Scott, W. G., and Cowtan, K. (2010) Features and development of Coot. *Acta Crystallogr. D Biol. Crystallogr.* **66,** 486–501 CrossRef Medline
50. Murshudov, G. N., Skubák, P., Lebedev, A. A., Pannu, N. S., Steiner, R. A., Nicholls, R. A., Winn, M. D., Long, F., and Vagin, A. A. (2011) REFMAC5 for the refinement of macromolecular crystal structures. *Acta Crystallogr. D Biol. Crystallogr.* **67,** 355–367 CrossRef Medline
51. Adams, P. D., Afonine, P. V., Bunkóczi, G., Chen, V. B., Davis, I. W., Echols, N., Headd, J. J., Hung, L.-W., Kapral, G. J., Grosse-Kunstleve, R. W., *et al*. (2010) PHENIX: a comprehensive Python-based system for macromolecular structure solution. *Acta Crystallogr. D Biol. Crystallogr.* **66,** 213–221 CrossRef Medline
52. Chen, V. B., Arendall, W. B., 3rd, Headd, J. J., Keedy, D. A., Immormino, R. M., Kapral, G. J., Murray, L. W., Richardson, J. S., and Richardson, D. C. (2010) MolProbity: all-atom structure validation for macromolecular crystallography. *Acta Crystallogr. D Biol. Crystallogr.* **66,** 12–21 CrossRef Medline
53. McCoy, A. J. (2007) Solving structures of protein complexes by molecular replacement with Phaser. *Acta Crystallogr. D Biol. Crystallogr.* **63,** 32–41 CrossRef Medline

54. Abergel, C. (2013) Molecular replacement: tricks and treats. *Acta Crystallogr. D Biol. Crystallogr.* **69,** 2167–2173 CrossRef Medline
55. Plumbridge, J. (2015) Regulation of the utilization of amino sugars by *Escherichia coli* and *Bacillus subtilis*: same genes, different control. *J. Mol. Microbiol. Biotechnol.* **25,** 154–167 CrossRef Medline
56. Kanehisa, M., Sato, Y., Kawashima, M., Furumichi, M., and Tanabe, M. (2016) KEGG as a reference resource for gene and protein annotation. *Nucleic Acids Res.* **44,** D457–D462 CrossRef Medline
57. North, R. A., Watson, A. J., Pearce, F. G., Muscroft-Taylor, A. C., Friemann, R., Fairbanks, A. J., and Dobson, R. C. (2016) Structure and inhibition of *N*-acetylneuraminate lyase from methicillin-resistant *Staphylococcus aureus*. *FEBS Lett.* **590,** 4414–4428 CrossRef
58. North, R. A., Kessans, S. A., Atkinson, S. C., Suzuki, H., Watson, A. J., Burgess, B. R., Angley, L. M., Hudson, A. O., Varsani, A., and Griffin, M. D. (2013) Cloning, expression, purification, crystallization and preliminary X-ray diffraction studies of *N*-acetylneuraminate lyase from methicillin-resistant *Staphylococcus aureus*. *Acta Crystallogr. F.* **69,** 306–312 CrossRef
59. North, R. A., Kessans, S. A., Griffin, M. D., Watson, A. J., Fairbanks, A. J., and Dobson, R. C. (2014) Cloning, expression, purification, crystallization and preliminary X-ray diffraction analysis of *N*-acetylmannosamine-6-phosphate 2-epimerase from methicillin-resistant *Staphylococcus aureus*. *Acta Crystallogr. F Struct. Biol. Commun.* **70,** 650–655 CrossRef
60. Pélissier, M.-C., Sebban-Kreuzer, C., Guerlesquin, F., Brannigan, J. A., Bourne, Y., and Vincent, F. (2014) Structural and functional characterization of the *Clostridium perfringens N*-acetylmannosamine-6-phosphate 2-epimerase essential for the sialic acid salvage pathway. *J. Biol. Chem.* **289,** 35215–35224 CrossRef Medline
61. Ryan, T. M., Trewhella, J., Murphy, J. M., Keown, J. R., Casey, L., Pearce, F. G., Goldstone, D. C., Chen, K., Luo, Z., Kobe, B., McDevitt, C. A., Watkin, S. A., Hawley, A. M., Mudie, S. T., Samardzic Boban, V., *et al.* (2018) An optimized SEC-SAXS system enabling high X-ray dose for rapid SAXS assessment with correlated UV measurements for biomolecular structure analysis. *J. Appl. Cryst.* **51,** 97–111 CrossRef
62. Ashkenazy, H., Abadi, S., Martz, E., Chay, O., Mayrose, I., Pupko, T., and Ben-Tal, N. (2016) ConSurf 2016: an improved methodology to estimate and visualize evolutionary conservation in macromolecules. *Nucleic Acids Res.* **44,** W344–W350 CrossRef Medline
63. Pettersen, E. F., Goddard, T. D., Huang, C. C., Couch, G. S., Greenblatt, D. M., Meng, E. C., and Ferrin, T. E. (2004) UCSF Chimera–a visualization system for exploratory research and analysis. *J. Comput. Chem.* **25,** 1605–1612 CrossRef Medline

The basis for non-canonical ROK family function in the *N*-acetylmannosamine kinase from the pathogen *Staphylococcus aureus*

David Coombes, James S. Davies, Michael C. Newton-Vesty, Christopher R. Horne, Thanuja G. Setty, Ramaswamy Subramanian, James W. B. Moir, Rosmarie Friemann, Santosh Panjikar, Michael D. W. Griffin, Rachel A. North and Renwick C. J. Dobson

J. Biol. Chem. 2020, 295:3301-3315.
doi: 10.1074/jbc.RA119.010526 originally published online January 15, 2020